A spiropyran with low pK_a for tracking DNA G-quadruplexes and revealing the dissipation of ΔΨm with senescence using an *in-situ* switching strategy

Xinrong Tian[a,1], Jin Li[a,b,1], Yanhui Zhang[a], Ying Gao[a], Muhammad Wasim Afzal[a], Aoli Wang[c], Tony D. James[d], Yinjuan Bai[a,*], Yuan Guo[a,*]

[a]*Key Laboratory of Synthetic and Natural Functional Molecule of the Ministry of Education, National Demonstration Center for Experimental Chemistry Education, College of Chemistry and Materials Science, Northwest University, Xi'an 710127, China*

[b]*College of Chemistry and Chemical Engineering, Xi'an University of Science and Technology, Xi'an, 710054, China*

[c]*High Magnetic Field Laboratory, Key Laboratory of High Magnetic Field and Ion Beam Physical Biology, Hefei Institutes of Physical Science, Chinese Academy of Sciences, Hefei 230031, China*

[d]*Department of Chemistry, University of Bath, Bath, BA2 7AY, United Kingdom*

[1]X. Tian and J. Li contributed equally to this work.

*Corresponding authors.

E-mail addresses: guoyuan@nwu.edu.cn (Y. Guo), baiyinjuan@nwu.edu.cn (Y. Bai).

Abstract

The *in-situ* fluorescence triggering of bioprobes only using endogenous bioforces is an ideal non-destructive real-time detection method, which is of particular interest to improve the accuracy of clinical diagnosis and treatment. We have recently reported a strategy of spiropyran *in-situ* switching triggered by endogenous biological forces *in vivo* to develop optical probes for this purpose. However, such probes, as with all spiropyrans, are sensitive to lysosomal acidity. We here present a spiropyran-based fluorescent probe **TANG** with low pK_a, which can recognize intranuclear DNA G4s *in situ* without the aid of exogenous light or chemicals and is as stable to lysosomal acidity due to a decreased pK_a value (4.3). Interestingly, despite the stability to lysosomal pH environment, the **TANG** spiropyran can be opened *in situ* by the negative membrane potential of extranuclear mitochondria (ΔΨm), causing a ratiometric change in fluorescence signals and providing the *in-situ* and real-time tracking of ΔΨm. Of note, ratiometric imaging using **TANG** indicates that ΔΨm decreases gradually with cellular senescence, which is to the best of our knowledge the first visualization of such mitochondrion-related aging processes using a ratiometric imaging approach.

Key words: Fluorescent probes; G-quadruplexes; Membrane potential of mitochondria; Senescence; Senescent cells.

1. Introduction

Spiropyrans, one of the most attractive families of photochromic compounds, undergo reversible structural isomerization between its initial ring-closed form and the open merocyanine form upon chemical stimulus, pH or light [1,2]. Owing to such unique photoswitchable and photochromic properties, over the past few years, a host of spiropyran-based derivatives have been developed and widely used in functional materials [3-11], chemical sensors [12-15], and for biological analysis [16-22]. A recent example of spiropyrans being used as functional materials was described by Roghani-Mamaqani and co-workers, where novel functionalized stimuli-responsive latex particles containing spiropyran were used as anticounterfeiting inks for writing on cellulosic paper and also the security marking of currency [23]. Spiropyrans are also suitable for biological applications. Bis-spiropyran ligands as dipolar molecule receptors and their application as *in vivo* glutathione fluorescent probes was first reported by the group of Yang and Chan [24]. While, Andréasson's group developed a spiropyran photoswitch which could be activated by UV light, the closed form exhibited no interaction with DNA while the open form was intercalated with DNA [25]. The group of Tian designed a unique bis-spiropyran-functionalized peptide sensor for real-time and reversible lysosomal tracking [26].

Although spiropyrans have been widely used for biomarker detection, there are still some limitations. Firstly, most of them are not stable to the acidity of lysosomes, which results in interference from lysosomes during the detection of other biological targets present in the cytoplasm (Fig. 1a). As such, in order to obtain stability to biological acidity, it is important to develop a spiropyran switch with a lower pK_a than the minimum pH of the lysosome (pH 4.5-6.0) [27-29]. Secondly, spiropyran switching molecules for the *in-situ* detection of biomarkers by endogenous bioforces are very limited since most spiropyran-based probes are controlled by light

irradiation, chemical stimulus or other exogenous stimuli. Furthermore, non-invasive *in-situ* recognition without external stimulation has outstanding advantages in obtaining *in-situ* and real-time high-fidelity information *in vivo* without disturbing the resting state of cells [30]. Therefore, functionalized spiropyrans with the ability to track different biomarkers *in situ* are urgently required.

Our interest in this area has been piqued by our recent success in developing spiropyran-linked fluorescent probes for the *in-situ* and real-time imaging and tracking of biomarkers including c-MYC DNA G-quadruplexes (G4s) and lysosomal pH [30,31]. The main advancements have been described in our previous report: (i) real-time detection due to rapid transport across live-cell and nuclear membranes of the hydrophobic closed spiropyran form, (ii) robust ratiometric imaging based on the resulting π-extended conjugation upon switching from closed to open, and (iii) an innovative bioforce-induced spiropyran *in-situ* switching (SIS) strategy for biomarkers. Specifically, SIS means that the spiropyran switching can be triggered by endogenous biological forces *in vivo* rather than exogenous light or chemicals to achieve the *in-situ* detection of biomarkers. However, such systems are sensitive to lysosomal acidity, as are other spiropyran-based bioprobes, and as such are limited to the tracking of c-MYC DNA G4s or lysosomal pH. These concerns encouraged us to consider a new SIS-based bioprobe without interference from lysosomal acidity for the *in-situ* and real-time detection of important biomarkers.

Considering that c-KIT DNA G4s are related to human gastrointestinal stromal tumor (GIST) [32] and tools to probe them are limited, herein we designed and synthesized a SIS-based fluorescent probe **TANG** with low pK_a for c-KIT DNA G4s using molecular docking and the introduction of multiple nitrogen atoms (Fig. 1b). As expected, **TANG** exhibits the best response towards c-KIT DNA G4s amongst various DNA G4s and is insensitive to lysosomal acidity due to

a decreased pK_a value (4.3). Surprisingly, although exhibiting stability to extranuclear lysosomes, **TANG** can be induced *in situ* by the negative membrane potential of mitochondria (ΔΨm) to be converted to the positively charged open form (**TANG-OPH**$^+$), resulting a significant red shift of 114 nm for emission bands. Live-cell fluorescence imaging indicates that **TANG** can be utilized for the *in-situ* and real-time tracking of intranuclear c-KIT DNA G4s and extranuclear mitochondrion membrane potential (Fig. 1b). It is believed that mitochondria play a central role in aging [33,34]. To our delight, using our **TANG** probe we could determine that ΔΨm dissipates gradually with cellular senescence.

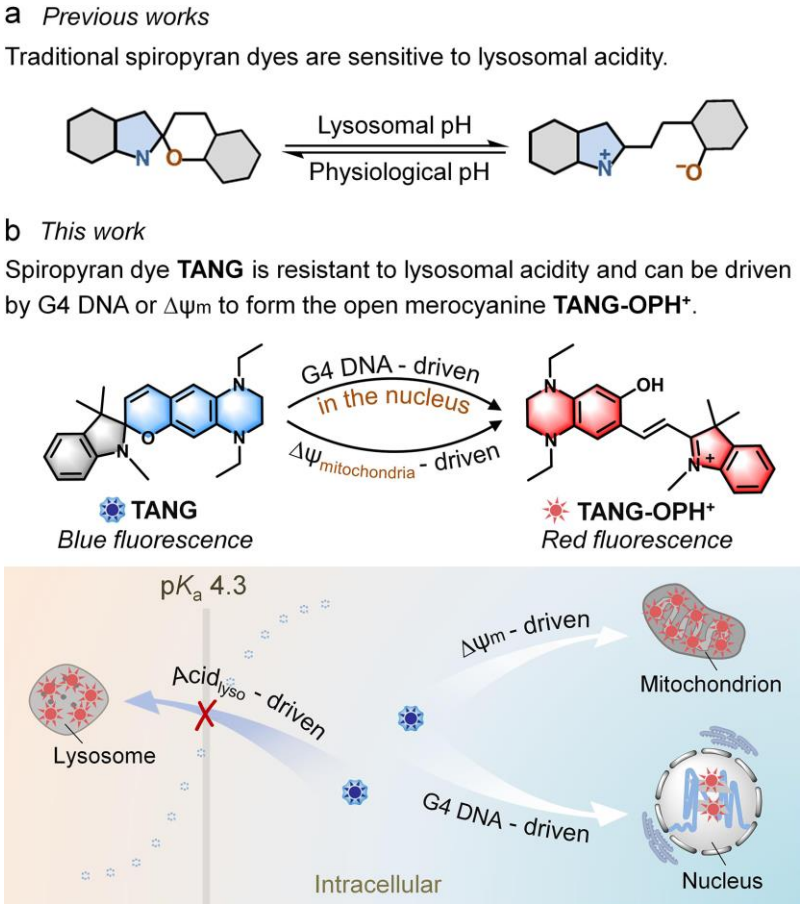

Fig. 1. (a) Illustration of traditional spiropyran dyes sensitive to lysosomal acidity. (b) Working principle of **TANG** with resistance to lysosomal acidity for sensing of G4 DNA or changes of ΔΨm resulting in the open merocyanine form **TANG-OPH**$^+$.

2. Experimental section

2.1. Materials and measurements

Reagents were gained from commercial sources and utilized without further distillation. XL413 was purchased from MedChemExpress (China, HY-15260A). GIST-48B cell lines were kindly provided by the group of Professor Jonathan A. Fletcher at Brigham and Women's Hospital in Boston. ^{1}H NMR and ^{13}C NMR spectra were obtained using a Varian Unity INOVA-400 spectrometer. High-resolution mass spectra (HRMS) were recorded on a Bruker micrOTOF-QII mass spectrometer (Germany). Infrared (IR) spectra were performed using a BrukerVertex 70 FI-IR spectrometer. X-ray crystallography with a Bruker SMART APEX-CCD system was employed to measure the single crystal structure. The fluorescence spectra were recorded on a Hitachi F-2700 fluorescence spectrometer (Japan) with a 1 mm quartz cuvette. UV-Vis absorption spectra were recorded on a Shimadzu UV-2550 spectrometer with a 10 mm quartz cuvette. Circular dichroism spectra were determined using a Chirascan Circular Dichroism Spectrometer (UK) with a 1 mm quartz cuvette. Cell images were observed using a Nikon A1 confocal microscopy.

2.2. Preparation of oligonucleotides

Oligonucleotide sequences are listed in Table S2. All the oligonucleotides were dissolved Tris-HCl buffer (25 mM, pH = 7.4) containing 20 mM KCl. Firstly, DNA G4s (c-KIT1, c-MYC, BCL-2 and 22AG) were heated to 90 ºC for 10 min, and then slowly cooled to room temperature. Secondly, two kinds of double-stranded DNA (ds-DNA1: ss-DNA1 and ss-DNA2; ds-DNA2: ss-DNA3 and ss-DNA4) were heated to 60 ºC for 10 min, and then slowly cooled to room temperature. Thirdly, one kind of double-stranded DNA (ct-DNA) and four kinds of single-stranded DNA were used directly without further heating. Lastly, the concentrations of DNA were identified by measuring the absorbance at 260 nm and appropriate molar extinction coefficients, which were

obtained by oligo analyzer from IDT (http://biophysics.idtdna.com/ UVSpectrum.html).

2.3. CellTiter-Glo® luminescent cell viability assay

80% Confluence GIST-48B, GIST-T1 and CHO (control) cells were seeded into a 96-well cell-culture plate with 100 μL per well. After incubating overnight at 37 °C under 5% CO_2, **TANG** with different concentrations (0, 0.3, 0.6, 1.3, 2.5, 5, 10 and 20 μM) were added to the wells. Then the cells were remained after incubation for 72 h. Then 10 μL CellTiter-Glo® reagent was added to each well. After standing for 10 min, luminescence was determined by Envision® Multilabel Plate-Reader. The inhibition rate was calculated by the formula:

$$\text{Inhibition rate} = 100\% - (RLU_P - RLU_B)/(RLU_D - RLU_B) \times 100\%$$

where RLU_P, RLU_D and RLU_B represent the luminescence of **TANG**, DMSO and background, respectively. Based on the data, nonlinear regression curve fitting was conducted through GraphPad Prism 6.0 simulation, which provides the values of GI50 (Table S3).

*2.4. Cell culture and **TANG** for confocal imaging in living cells*

GIST-48B, A375, Hela, SMMC-7721 and A549 cells were cultured on glass bottom Petri dishes for 3 days in DMEM containing 15% FBS and 1% penicillin-streptomycin in 5% CO_2 and 95% air at 37 ºC. The cells were washed with PBS three times and then stained with **TANG** (20 μM), respectively. Then all the cell images were acquired on a confocal laser-scanning microscopy (Nikon A1). Blue channel: Ex/Em = 405/425-475 nm; red channel: Ex/Em = 561/570-620 nm; NIR channel: Ex/Em = 640/663-738 nm.

3. Results and discussion

3.1. Design and synthesis

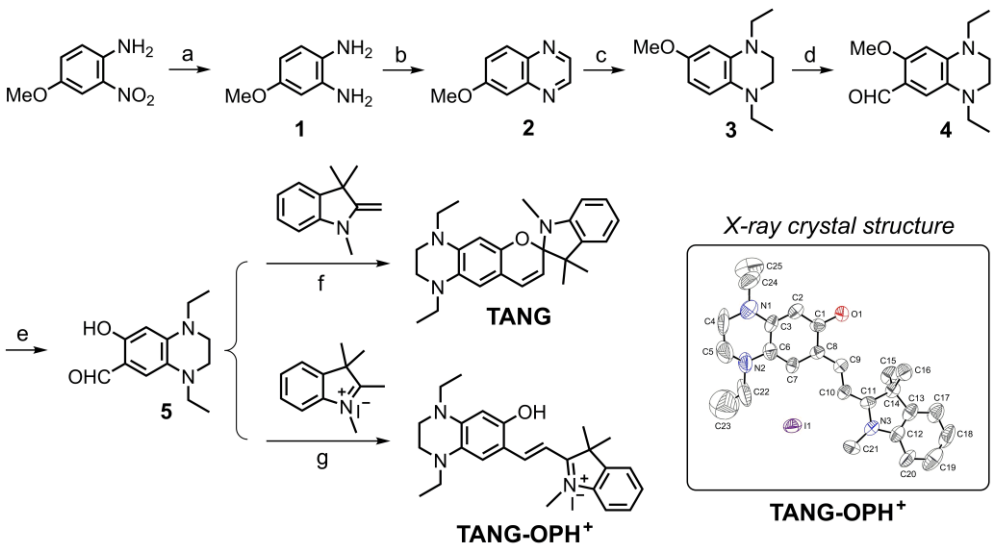

Scheme 1. Synthetic routes for probe **TANG** and its open form **TANG-OPH**$^+$. Reagents and conditions: (a) Fe/acetic acid, 120 °C; (b) Glyoxal, acetonitrile, 60 °C; (c) Toluene, $NaBH_4$, acetic acid, 0 °C to rt, then reflux; (d) $POCl_3$/DMF, 75 °C; (e) Al/I_2, acetonitrile, reflux; (f) Ethanol, reflux.

Utilizing molecular docking and multi-nitrogen ring fusion strategies, **TANG** was rationally designed to be able to respond c-KIT1 G4 DNA in a ratiometric fluorescence manner and to be insensitive to lysosomal acidity. The docking results indicated that in the groove region **TANG** binds to c-KIT1 G4 DNA formed by a 22 base G-rich sequence in a nuclease hypersensitive region of the c-KIT promoter DNA (Fig. 2a,b). The lipophilic and uncharged probe interacts with c-KIT1 G4 DNA through π-π stacking and hydrophobic interactions, generating the corresponding docking binding energy of −52.5 kcal/mol (Table S1). However, **TANG-OPH**$^+$ in the charged open form has a planar, aromatic and polycyclic structure suitable for enhanced DNA binding. The positive charge of **TANG-OPH**$^+$ facilitates DNA binding through electrostatic attraction with the negatively charged phosphate backbone and loops of the G4 DNA. As expected, π-π stacking between the phenyl ring of tetrahydroquinoxaline scaffold and the pyrimidine ring of DA-19 and hydrophobic interactions give a binding energy of -59.4 kcal/mol. In addition, a hydrogen bonding

network and electrostatic binding interactions between N^+ with π-electron of the double ring of DG-4 result in a binding energy of -75.4 kcal/mol (Table S1). These results indicate that **TANG-OPH**$^+$ binds to c-KIT1 G4 DNA with significantly higher affinity than **TANG** does, which provides a potential bioforce where c-KIT1 DNA G4s can induce switching from **TANG** to **TANG-OPH**$^+$ *in situ.* **TANG** and its open form **TANG-OPH**$^+$ were synthesized *via* six steps from commercial chemicals, and the X-ray crystal structure of **TANG-OPH**$^+$ was obtained (Scheme 1 and Table S4).

*3.2. Spectral response of **TANG** to c-KIT1 G4 DNA*

In this section, our investigation began with the selectivity of **TANG** towards various DNA. As seen from Fig. 2c, **TANG** showed high selectivity for DNA G4s over single-stranded DNA and double-stranded DNA. Among these DNA G4s, **TANG** had the best response to c-KIT1 DNA G4s with a 63-fold enhancement at 573 nm because of its structure and size suitable for binding with this DNA G4s, which is in good agreement with the results obtained from the molecular docking. Next, we focused on the spectral response of **TANG** to c-KIT1 G4 DNA. Under physiological conditions (Tris-HCl/KCl buffer, pH 7.4), the probe exhibited a relatively high fluorescence band centered at 459 nm and fluorescence emission in the red region was not observed (Fig. 2d), indicating that in this system the closed form exists. Interestingly, after addition of c-KIT1 G4 DNA, a new emission band centered at 573 nm was observed (Fig. 2d), and its intensity rapidly increased with the amount of c-KIT1 G4 DNA increasing (Fig. 2e). Based on the previous results from our group, we reasoned that the new emission at 573 nm in the above system emerged not only because of an increase in concentration of the open form **TANG-OPH**$^+$ but also the binding of **TANG** and c-KIT1 G4 DNA resulting in increased rigidity. Moreover, from the

plot of the fluorescence titration, an excellent linearity (R^2 = 0.993) was observed over a concentration range of 0-10 μM (Fig. 2e, inset).

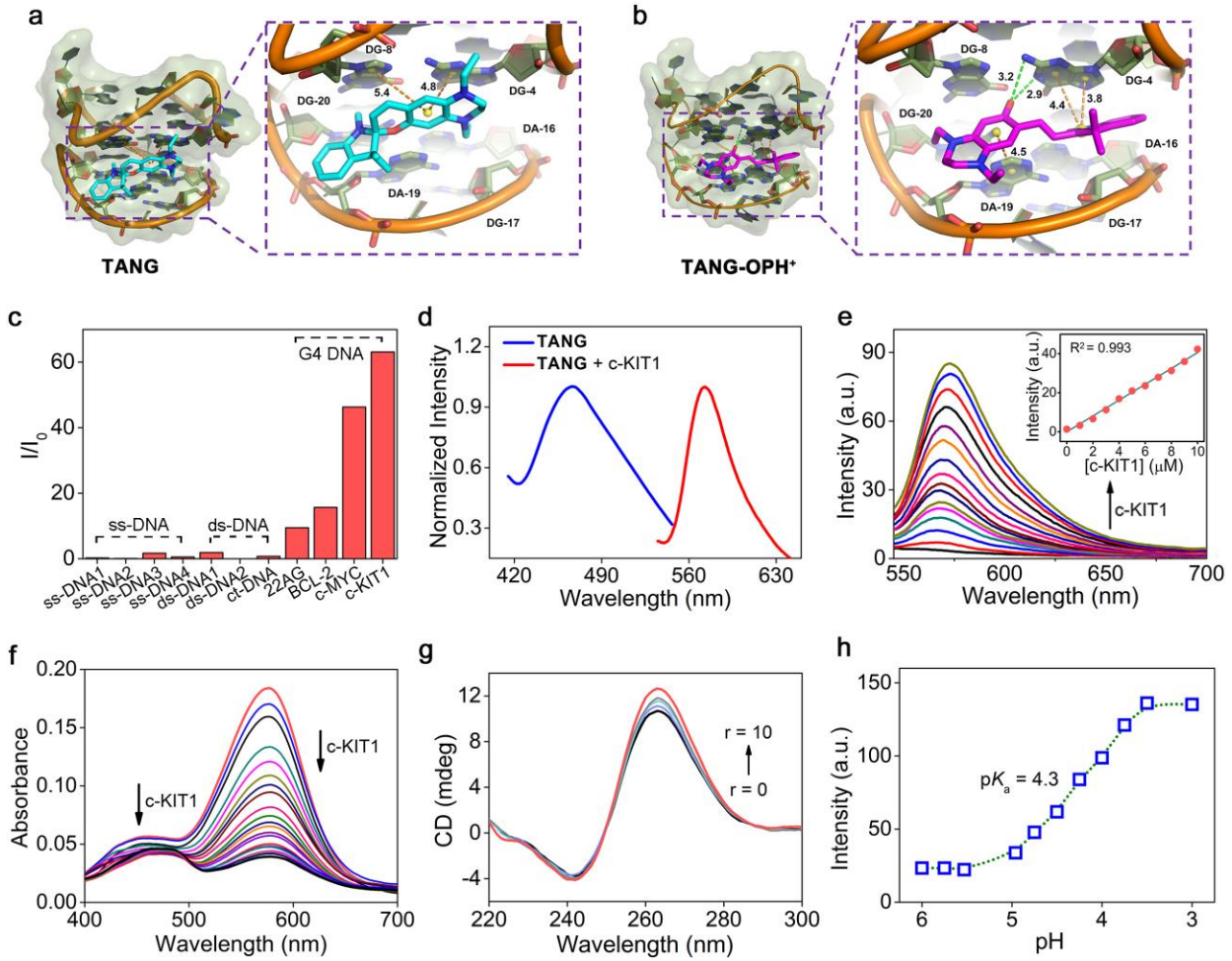

Fig. 2. (a,b) The molecular docking model of **TANG** with c-KIT1 G4 DNA (a) and **TANG-OPH**$^+$ with c-KIT1 G4 DNA (b), respectively (PDB ID: 2O3M). (c) Fluorescence intensity at 573 nm of **TANG** (10 μM) with different nucleic acids (10 μM) including single-stranded DNA (ss-DNA1, ss-DNA2, ss-DNA3 and ss-DNA4), double-stranded DNA (ds-DNA1, ds-DNA2 and ct-DNA), telomere G-quadruplex DNA (22AG; promoter) and G-quadruplex DNA (BCL-2, c-MYC and c-KIT1). I and I_0 represent the fluorescence intensity at 573 nm of **TANG** containing DNA or not. (d) Normalized emission of **TANG** (10 μM) (λ_{ex} = 400 nm) and the reaction solution of **TANG** (10 μM) with c-KIT1 G4 DNA (15 μM) (λ_{ex} = 520 nm) in Tris-HCl buffer (25 mM, pH 7.4,

containing 20 mM KCl). (e) Fluorescence spectra of **TANG** (10 μM) upon titration with c-KIT1 G4 DNA (0-15 μM) in Tris-HCl buffer (25 mM, pH 7.4, containing 20 mM KCl). Inset: linear relationship between fluorescence intensity of **TANG** and concentrations of c-KIT1 G4 DNA. (f) UV-Vis spectra of **TANG** (10 μM) upon titration with c-KIT1 G4 DNA (0-20 μM) in Tris-HCl buffer (25 mM, pH 7.4, containing 20 mM KCl). (g) CD spectra recorded for c-KIT1 G4 DNA (10 μM) upon titration with **TANG** in Tris-HCl buffer. r = [**TANG**]/[c-KIT1 G4 DNA] (0, 2.5, 5, 7.5 and 10). (h) Fluorescence intensity at 573 nm of **TANG** (10 μM) in sodium phosphate buffer (100 mM) with different pH values.

The interaction of the probe **TANG** with c-KIT1 G4 DNA was also investigated using absorption spectral titrations. **TANG** exhibited a characteristic absorption profile centered at 461 nm and 578 nm (Fig. 2f), respectively. On addition of c-KIT1 G4 DNA, a bathochromic shift of 14 nm and 16% hypochromicity at short wavelength (461 nm) was observed. In comparison, a very strong hypochromic effect (76%) along with a bathochromic shift (8 nm) at long wavelength (578 nm) was observed. This indicated that the open form **TANG-OPH**$^+$ with π-extended conjugation had a higher affinity for c-KIT1 G4 DNA than **TANG**.

Circular dichroism (CD) spectroscopy is a useful technology to determine the conformation of G4 DNA structures in solution and to study the effect of ligand binding on G4 structures [35]. Consequently, we exploited the technique to explore the structural changes of c-KIT1 G4 DNA after the interaction with **TANG**. C-KIT1 G4 DNA displayed a negative peak at ~240 nm and a positive peak at ~260 nm, which corresponded to the parallel topology (Fig. 2g). Upon the addition of **TANG**, no changes of characteristic peaks were observed only an increase of the peaks' ellipticities, indicating that **TANG** could interact with c-KIT1 G4 DNA and did not change the DNA structure in pH 7.4 buffer.

Interestingly, the fluorescence and CD spectroscopy of c-KIT1 G4 DNA/**TANG** complex system changed at pH 4.0. As illustrated in Fig. S1a, the fluorescence emission maximum at 573 nm was observed in the absence of c-KIT1 G4 DNA in phosphate buffer (100 mM, pH 4.0), indicating the appearance of the open form of **TANG**. Under these conditions, the fluorescence intensity enhanced dramatically on the addition of c-KIT1 G4 DNA, and was significantly higher than those at pH 7.4. Subsequently, the structural modification of c-KIT1 G4 DNA upon binding with **TANG** in phosphate buffer (100 mM, pH 4.0) was examined using the CD spectra. Most noticeably, from Fig. S1b, besides the two original peaks, a new peak appeared at ~295 nm without adding **TANG**, which is a signature for mixed types of G4s. Of note, the ellipticities at ~295 nm gradually decreased and disappeared with the continuous addition of **TANG** and significant enhancements of the bands near 240 and 265 nm were observed, which indicates that the structure of c-KIT1 G4 DNA changed from mixed to parallel conformation. These results demonstrated that **TANG** exhibits strong interactions with c-KIT1 G4 DNA and forces the mixed topological structures of the G4 DNA to adopt a parallel structure under acid conditions.

In general, spiropyrans can be converted to the open form at a certain pH and are sensitive to lysosomal acidity. Here, to evaluate the lysosomal-acidic resistance of **TANG**, the effect of acid over a pH range from 3 to 6 was evaluated. Compared with common spiropyrans including **QIN** which we reported previously [30], **TANG** can be transformed into its protonated open form **TANG-OPH**$^+$ at a low pH. Next, the pK_a of **TANG** was determined to be 4.3 (Fig. 2h). This low pK_a value indicated that it is difficult for **TANG** to be isomerized at the pH of lysosomes.

3.3. Visualization of endogenous DNA G4s in living cells

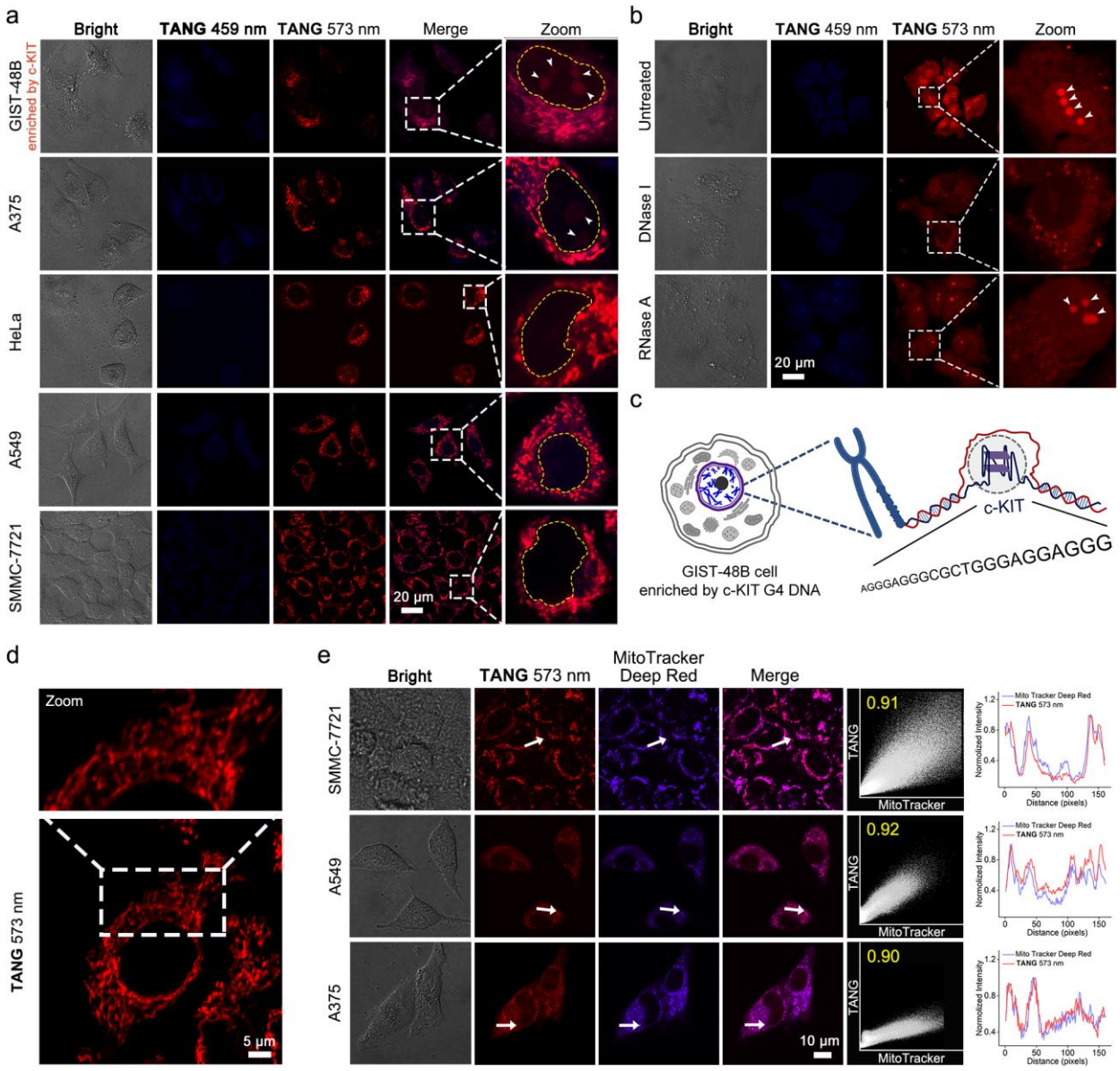

Fig. 3. (a) Confocal images of c-KIT1 G4 DNA in living cancer cells (GIST-48B, A375, HeLa, A549 and SMMC-7721) stained with **TANG** (20 μM). (b) "DNA/RNA digestion" confocal images of fixed GIST-48B cells stained with **TANG** (20 μM) without (upper, untreated) and with DNase I (middle) or RNase A treatment (lower). (c) Schematic illustration of GIST-48B cell enriched by c-KIT G4 DNA. (d) Confocal image of living SMMC-7721 cells stained by **TANG** (20 μM, lower); The zoomed image (upper). (e) Co-localization studies of living SMMC-7721, A549 and A375 cells stained by MitoTracker Deep Red FM (100 nM) and **TANG** (20 μM). the intensity

scatter plots of MitoTracker Deep Red FM and **TANG**; Intensity profiles of MitoTracker Deep Red FM (arrows in NIR channels) and **TANG** 573 nm (arrows in red channels) in the regions of interest (ROIs) across the three kinds of cells. Scale bars: 20 μm (a and b), 5 μm (d) and 10 μm (e). Blue channel (**TANG** 459 nm): Ex/Em = 405/425-475 nm; red channel (**TANG** 573 nm): Ex/Em = 561/570-620 nm; NIR channel: Ex/Em = 640/663-738 nm.

The cytotoxicity of **TANG** was evaluated by using a CellTiter-Glo® luminescent cell viability assay in GIST-48B and GIST-T1 cells with overexpression of c-KIT G4s [32], and CHO (control) cells. As shown in Table S3, compared with CHO cells, **TANG** had no significant antiproliferation efficacies against GIST-48B and GIST-T1 cells, suggesting that the probe was biocompatible and could be used for cell imaging. Then GIST-48B and A375 cells with c-KIT G4s overexpression were selected as the positive cell models [32,36], while HeLa, A549 and SMMC-7721 cells were selected as controls due to lower expression of c-KIT G4s. We then used **TANG** to visualize endogenous DNA G4s in the above living cells. Confocal images exhibited the blue fluorescence of **TANG** in these cells (Fig. 3a). While, red fluorescence signals were observed in the nuclei of both GIST-48B and A375 cells containing abundant c-KIT G4s forming sequences. The results demonstrate that **TANG** was induced to open to its red fluorescent form *in situ* by DNA G4s. To further verify whether **TANG** binds to G4 DNA, we performed DNA digest experiments with deoxyribonuclease I (DNase I) and ribonuclease A (RNase A). The red fluorescence signals of **TANG** in nuclei diminished remarkably after digestion by DNase I, but there is no significant difference after RNase treatment (Fig. 3b). These experiments confirmed that **TANG** specifically targeted the two kinds of cancer cells enriched by c-KIT G4 DNA (Fig. 3a-c).

3.4. Subcellular localization

In addition to the red fluorescence signals in the nuclei, red fluorescence was also observed the

cytoplasm of all the cells (Fig. 3a), which was surprising given that **TANG** should be acid resistant and as such should not be opened in the cytoplasm. After further investigation, the red stained regions showed numerous rod-like and filament-like structures, suggesting that the low-pK_a spiropyran probe **TANG** accumulates in the mitochondria (Fig. 3d). To evaluate the mitochondrion-targeting performance of **TANG**, co-localization experiments were performed. SMMC-7721, A549 and A375 cells were costained with both **TANG** and MitoTracker Deep Red FM (a commercial mitochondrion NIR probe) or LysoTracker Deep Red (a commercial lysosome NIR probe) at 37 °C. Confocal images indicated that the fluorescence of the probe at 573 nm overlaid that of MitoTracker Deep Red FM (Fig. 3e). The Pearson's correlation coefficients (PCCs) were 0.91, 0.92 and 0.90, respectively. There are variations in close synchrony in the emission intensity profiles of **TANG** and MitoTracker Deep Red FM within the linear regions of interest (ROIs) (Fig. 3e). In contrast, the probe did not significantly target lysosomes with the low PCC value of 0.66 from co-localization image of **TANG** and LysoTracker Deep Red (Fig. S2). These results indicated that the SIS-based probe **TANG** with low pK_a exhibits the unique ability to label mitochondria selectively rather than lysosomes.

3.5. Tracking the changes of ΔΨm

Since **TANG** can be selectively switched to its open form in mitochondria with a blue-to-red ratiometric fluorescence response, we reasoned that the negative ΔΨm (-120 to -180 mV) [37] of cellular mitochondria gives rise to the switching of **TANG** to positively charged **TANG-OPH$^+$**. To prove our speculation, the change of fluorescence signal of **TANG** with ΔΨm was then investigated. Carbonyl cyanide *m*-chlorophenylhydrazone (CCCP), a mitochondria uncoupler [38-40], was utilized to induce a decrease of ΔΨm in living SMMC-7721 cells. From Fig. 4a,b and Fig. S3, the fluorescence intensity in the red channel decreased significantly, whereas that in the

blue channel enhanced gradually with CCCP treatment time, confirming that **TANG** can be switched *in situ* by the ΔΨm electrostatic bioforce into **TANG-OPH**$^{+}$ in the mitochondria. Next, we investigated the capability of **TANG** for the real-time tracking of mitochondria in SMMC-7721 cells. As expected, red fluorescence was observed within 15 s (Fig. 4c and Fig. S4), which suggested that **TANG** can rapidly penetrate membranes and switch *in situ* to its open form in mitochondria, consequently promoting the imaging of mitochondria in real time.

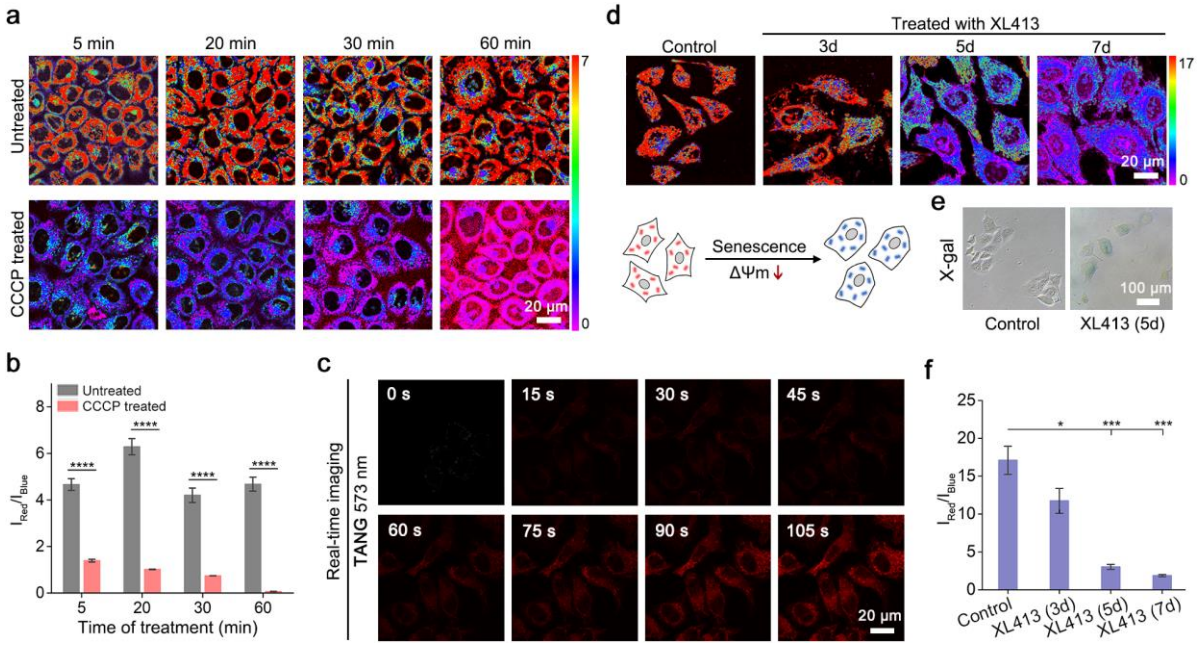

Fig. 4. (a) The ratio images of SMMC-7721 cells untreated (upper) or treated by CCCP (lower, 30 μM) for different times and then stained with **TANG** (20 μM). (b) Quantification of fluorescence intensity ratios (I_{Red}/I_{Blue}). (c) Confocal images of SMMC-7721 cells stained with **TANG** (20 μM) at different times. (d) The ratio images of HepG2 cells untreated or treated by XL413 (5 μM) at different time intervals (3 days, 5 days and 7 days) and stained by **TANG** (20 μM) before imaging. (e) Images after staining by an established X-gal assay of control and XL413-treated to verfiy SA-β-gal expression. (f) Quantification of fluorescence intensity ratios (I_{Red}/I_{Blue}). Scale bars: 20 μm (a, c and d) and 100 μm (e). Blue channel (**TANG** 459 nm): Ex/Em = 405/425-475 nm; red channel

(**TANG** 573 nm): Ex/Em = 561/570-620 nm. Error bars indicated the mean value (n=3) ± standard deviation (S.D.). Significant differences (*P < 0.05, ***P < 0.001, ****P < 0.0001) are analyzed by two-sided Student's *t*-test.

Encouraged by the ΔΨm tracking capability of **TANG**, changes of ΔΨm with cellular senescence were further monitored. Here we took senescent HepG2 cells as a senescent cell model, in which DNA-replication kinase CDC7 inhibitor XL413 was utilized to stimulate HepG2 cells senescence. [41] The senescence of these cells was confirmed by the X-gal staining assay (Beyotime Biotechnology) (Fig. 4e), which is a general method to evaluate cellular senescence. HepG2 cells were treated with XL413 for different times and then incubated with **TANG** for imaging by confocal microscopy. As shown in Fig. 4d and Fig. S5, compared with the control cells, the XL413-treated cells at different times exhibited an obvious time-dependent increase in the blue channel and decrease in the red channel. Meanwhile the ratio of the average fluorescence intensity (I_{Red}/I_{Blue}) was calculated, and the ratio values decreased from about 17.1 to 1.9 (Fig. 4f). This proved that ΔΨm dissipates gradually with cellular senescence, which was visualized for the first time using ratiometric imaging.

4. Conclusion

Altogether, we have demonstrated that **TANG**, designed by molecular docking and a unique low-pK_a spiropyran *in-situ* switching strategy, could be used for the real-time ratiometric tracking of DNA G4s, especially c-KIT DNA G4s. Because the pK_a value is 4.3, **TANG** overcomes the pH sensitivity limitation of traditional spiropyran-linked probes. Somewhat surprisingly, our lysosomal-acidity resistant probe could be activated *in situ* by the negative membrane potential of mitochondria to form the red-emitting (573 nm) open form from the blue-emitting (459 nm) closed form, achieving the real-time ratiometric detection of the membrane potential of mitochondria

located in live-cell cytoplasm. Given the central role of mitochondria in aging, **TANG** has been used to study the changes of ΔΨm with aging. Imaging results using our **TANG** probe indicate that ΔΨm dissipates with cellular senescence. Our SIS-based probe with low pK_a for real-time ratiometric sensing of both intranuclear DNA G4s and extranuclear mitochondrion membrane potential is unprecedented and will pave the way for probing aging and G4s-related diseases.

Declaration of Competing Interest

The authors report no declarations of interest.

Acknowledgments

We gratefully appreciate the financial support from NSF of China (21977082 and 22037002), the Natural Science Basic Research Plan in Shaanxi Province (2020JC-38), the Technology Plan Project of Xi'an (2019218214GXRC018CG019-GXYD18.1). GIST-48B cell lines were kindly provided by the group of Professor Jonathan A. Fletcher at Brigham and Women's Hospital in Boston. Tony D. James wishes to thank the Royal Society for a Wolfson Research Merit Award.

References

[1] L. Kortekaas, W.R. Browne, The evolution of spiropyran: fundamentals and progress of an extraordinarily versatile photochrome. Chem. Soc. Rev. 48 (12) (2019) 3406-3424, https://doi.org/10.1039/C9CS00203K.

[2] A.A. Ali, R. Kharbash, Y. Kim, Chemo- and biosensing applications of spiropyran and its derivatives - A review. Anal. Chim. Acta 1110 (2020) 199-223, https://doi.org/10.1016/j.aca.2020.01.057.

[3] Klajn, R. Spiropyran-based dynamic materials. Chem. Soc. Rev. 43 (1) (2014) 148-184, https://doi.org/10.1039/C3CS60181A.

[4] L. Wang, Y. Feng, Y. Zhou, M. Jia, G. Wang, W. Guo, L. Jiang, Photo-switchable two-dimensional nanofluidic ionic diodes, Chem. Sci. 8 (6) (2017) 4381-4386, https://doi.org/10.1039/C7SC00153C.

[5] L. Wang, Q. Li, Photochromism into nanosystems: towards lighting up the future nanoworld. Chem. Soc. Rev. 47 (3) (2018) 1044-1097, https://doi.org/10.1039/C7CS00630F.

[6] A.B. Kanj, A. Chandresh, A. Gerwien, S. Grosjean, S. Bräse, Y. Wang, H. Dube, L. Heinke, Proton-conduction photomodulation in spiropyran-functionalized MOFs with large on-off ratio. Chem. Sci. 11 (5) (2020) 1404-1410, https://doi.org/10.1039/C9SC04926F.

[7] M. Ghani, A. Heiskanen, J. Kajtez, B. Rezaei, N.B. Larsen, P. Thomsen, A. Kristensen, A. Zukauskas, M. Alm, J. Emneus, On-demand reversible UV-triggered interpenetrating polymer net-work-based drug delivery

system using the spiropyran-merocyanine hydrophobicity switch. ACS Appl. Mater. Interfaces 13 (3) (2021) 3591-3604, https://dx.doi.org/10.1021/acsami.0c19081.

[8] M. Tao, X. Liang, J. Guo, S. Zheng, Q. Qi, Z. Cao, Y. Mi, Z. Zhao, Dynamic photochromic polymer nanoparticles based on matrix-dependent förster resonance energy transfer and aggregation-Induced emission properties. ACS Appl. Mater. Interfaces 13 (28) (2021) 33574-33583, https://doi.org/10.1021/acsami.1c09677.

[9] H. Qiu, S. Ippolito, A. Galanti, Z. Liu, P. Samorì, Asymmetric dressing of WSe2 with (macro)molecular switches: fabrication of quaternary-responsive transistors. ACS Nano 15 (6) (2021) 10668-10677, https://doi.org/10.1021/acsnano.1c03549.

[10] Y. Huang, H.K. Bisoyi, S. Huang, M. Wang, X.-M. Chen, Z. Liu, H. Yang, Q. Li, Bioinspired synergistic photochromic luminescence and programmable liquid crystal actuators. Angew. Chem. Int. Ed. 60 (20) (2021) 11247-11251, https://doi.org/10.1002/anie.202101881.

[11] Z. Wu, Q. Wang, P. Li, B. Fang, M. Yin, Photochromism of neutral spiropyran in the crystalline state at room temperature. J. Mater. Chem. C 9 (19) (2021) 6290-6296, https://doi.org/10.1039/D1TC00974E.

[12] N. Shao, H. Wang, X.D. Gao, R.H. Yang, W.H. Chan, Spiropyran-based fluorescent anion probe and its application for urinary pyrophosphate detection. Anal. Chem. 82 (11) (2010) 4628-4636, https://doi.org/10.1021/ac1008089.

[13] R. Zhang, L. Hu, Z. Xu, Y. Song, H. Li, X. Zhang, X. Gao, M. Wang, C. Xian, A highly selective probe for fluorescence turn-on detection of Fe^{3+} ion based on a novel spiropyran derivative. J. Mol. Struct. 1204 (2020) 127481, https://doi.org/10.1016/j.molstruc.2019.127481.

[14] T.T.K. Cuc, P.Q. Nhien, T.M. Khang, C.-C. Weng, C.-H Wu, B.B. Hue, Y.-K. Li, J.I. Wu, H.-C. Lin, Optimization of FRET behavior in photoswitchable [2]rotaxanes containing bifluorophoric naphthalimide donor and merocyanine acceptor with sensor approaches toward sulfite detection. Chem. Mater. 32 (21) (2020) 9371-9389, https://doi.org/10.1021/acs.chemmater.0c03314.

[15] T. Zhang, F. Huo, W. Zhang, J. Chao, C. Yin, Ultra-pH-sensitive sensor for visualization of lysosomal autophagy, drug-induced pH alteration and malignant tumors microenvironment. Sens. Actuators B Chem. 345 (2021) 130393, https://doi.org/10.1016/j.snb.2021.130393.

[16] X. Zhang, J. Zhang, Y.-L. Ying, H. Tian, Y.-T. Long, Single molecule analysis of light-regulated RNA: spiropyran interactions. Chem. Sci. 5 (7) (2014) 2642-2646, https://doi.org/10.1039/C4SC00134F.

[17] H. Zhang, C. Wang, T. Jiang, H. Guo, G. Wang, X. Cai, L. Yang, Y. Zhang, H. Yu, H. Wang, K. Jiang, Microtubule-targetable fluorescent probe: site-specific detection and super-resolution imaging of ultratrace tubulin in microtubules of living cancer cells. Anal. Chem. 87 (10) (2015) 5216-5222, https://doi.org/10.1021/acs.analchem.5b01089.

[18] T. Bai, A. Sinclair, F. Sun, P. Jain, H.-C. Hung, P. Zhang, J.-R. Ella-Menye, W. Liu, S. Jiang, Harnessing isomerization-mediated manipulation of nonspecific cell/matrix interactions to reversibly trigger and suspend stem cell differentiation. Chem. Sci. 7 (1) (2016) 333-338, https://doi.org/10.1039/C5SC03244J.

[19] C. Wang, G. Wang, X. Li, K. Wang, J. Fan, K. Jiang, Y. Guo, H. Zhang, Highly sensitive fluorescence molecular switch for the ratio monitoring of trace change of mitochondrial membrane potential. Anal. Chem. 89 (21) (2017) 11514-11519, https://doi.org/10.1021/acs.analchem.7b02781.

[20] J. Ji, X. Li, T. Wu, F. Feng, Spiropyran in nanoassemblies as a photosensitizer for photoswitchable ROS generation in living cells, Chem. Sci. 9 (26) (2018) 5816-5821, https://doi.org/10.1039/C8SC01148F.

[21] S.J. Park, V. Juvekar, J.H. Jo, H.M. Kim, Combining hydrophilic and hydrophobic environment sensitive dyes to detect a wide range of cellular polarity. Chem. Sci. 11 (2) (2020) 596-601, https://doi.org/10.1039/C9SC04859F.

[22] Y. Cong, X. Wang, S. Zhu, L. Liu, L. Li, Spiropyran-functionalized gold nanoclusters with photochromic ability for light-controlled fluorescence bioimaging. ACS Appl. Bio. Mater. 4 (3) (2021) 2790-2797, https://doi.org/10.1021/acsabm.1c00011.

[23] A. Abdollahi, K. Sahandi-Zangabad, H. Roghani-Mamaqani, Rewritable anticounterfeiting polymer inks based on functionalized stimuli-responsive latex particles containing spiropyran photoswitches: reversible photopatterning and security marking, ACS Appl. Mater. Interfaces 10 (45) (2018) 39279-39292, https://doi.org/10.1021/acsami.8b14865.

[24] N. Shao, J. Jin, H. Wang, J. Zheng, R. Yang, W. Chan, Z. Abliz, Design of bis-spiropyran ligands as dipolar molecule receptors and application to *in vivo* glutathione fluorescent probes, J. Am. Chem. Soc. 132 (2) (2010) 725-736, https://doi.org/10.1021/ja908215t.

[25] J. Andersson, S. Li, P. Lincoln, J. Andréasson, Photoswitched DNA-binding of a photochromic spiropyran, J. Am. Chem. Soc. 130 (36) (2008) 11836-11837, https://doi.org/10.1021/ja801968f.

[26] L. Chen, J. Wu, C. Schmuck, H. Tian, A switchable peptide sensor for real-time lysosomal tracking, Chem. Commun. 50 (49) (2014) 6443-6446, https://doi.org/10.1039/C4CC00670D.

[27] F. Galindo, M.I. Burguete, L. Vigara, S.V. Luis, N. Kabir, J. Gavrilovic, D.A. Russell, Synthetic macrocyclic peptidomimetics as tunable pH probes for the fluorescence imaging of acidic organelles in live cells, Angew. Chem. Int. Ed. 44 (40) (2005) 6504-6508, https://doi.org/10.1002/anie.200501920.

[28] Y. Wang, J. Li, L. Feng, J. Yu, Y. Zhang, D. Ye, H.-Y. Chen, Lysosome-targeting fluorogenic probe for cathepsin B imaging in living cells, Anal. Chem. 88 (24) (2016) 12403-12410, https://doi.org/10.1021/acs.analchem.6b03717.

[29] M. Grossi, M. Morgunova, S. Cheung, D. Scholz, E. Conroy, M. Terrile, A. Panarella, J.C. Sompson, W.M. Gallagher, D.F. O'Shea, Lysosome triggered near-infrared fluorescence imaging of cellular trafficking processes in real time, Nat. Commun. 7 (2016) 10855, https://doi.org/10.1038/ncomms10855.

[30] J. Li, X. Yin, B. Li, X. Li, Y. Pan, J. Li, Y. Guo, Spiropyran *in situ* switching: A real-time fluorescence strategy for tracking DNA G-quadruplexes in live cells, Anal. Chem. 91 (8) (2019) 5354-5361, https://doi.org/10.1021/acs.analchem.9b00436.

[31] J. Li, X. Li, J. Jia, X. Chen, Y. Lv, Y. Guo, J. Li, A ratiometric near-infrared fluorescence strategy based on spiropyran *in situ* switching for tracking dynamic changes of live-cell lysosomal pH, Dyes Pigm. 166 (2019) 433-442, https://doi.org/10.1016/j.dyepig.2019.03.060.

[32] S. Sakurai, T. Fukasawa, J.-M. Chong, A. Tanaka, M. Fukayama, C-kit gene abnormalities in gastrointestinal stromal tumors (tumors of interstitial cells of cajal). Jpn. J. Cancer Res. 90 (12) (1999) 1321-1328, https://doi.org/10.1111/j.1349-7006.1999.tb00715.x.

[33] A.L. Hughes, D.E. Gottschling, An early age increase in vacuolar pH limits mitochondrial function and lifespan in yeast. Nature 492 (2012) 261-265, https://doi.org/10.1038/nature11654.

[34] C. Correia-Melo, F.D. Marques, R. Anderson, G. Hewitt, R. Hewitt, J. Cole, B.M. Carroll, S. Miwa, J. Birch, A. Merz, M.D. Rushton, M. Charles, D. Jurk, S.W. Tait, R. Czapiewski, L. Greaves, G. Nelson, M. Bohlooly-Y, S. Rodriguez-Cuenca, A. Vidal-Puig, D. Mann, G. Saretzki, G. Quarato, D.R. Green, P.D. Adams,

T.V. Zglinicki, V.I. Korolchuk, J.F. Passos, Mitochondria are required for pro-ageing features of the senescent phenotype, EMBO J. 35 (7) (2016) 724-742, https://doi.org/10.15252/embj.201592862.

[35] P. Murat, Y. Singh, E. Defrancq, Methods for investigating G-quadruplex DNA/ligand interactions. Chem. Soc. Rev. 40 (11) (2011) 5293-5307, https://doi.org/10.1039/C1CS15117G.

[36] P.G. Natali, M.R. Nicotra, A.B. Winkler, R. Cavaliere, A. Bigotti, A. Ullrich, Progression of human cutaneous melanoma is associated with loss of expression of c-kit proto-oncogene receptor. Int. J. Cancer 52 (2) (1992) 197-201, https://doi.org/10.1002/ijc.2910520207.

[37] Y. Liu, J. Zhou, L. Wang, X. Hu, X. Liu, M. Liu, Z. Cao, D. Shangguan, W. Tan, A cyanine dye to probe mitophagy: simultaneous detection of mitochondria and autolysosomes in live cells, J. Am. Chem. Soc. 138 (38) (2016) 12368-12374, https://doi.org/10.1021/jacs.6b04048.

[38] Y. Chen, C. Zhu, J. Cen, Y. Bai, W. He, Z. Guo, Ratiometric detection of pH fluctuation in mitochondria with a new fluoresce-in/cyanine hybrid sensor. Chem. Sci. 6 (5) (2015) 3187-3194, https://doi.org/10.1039/C4SC04021J.

[39] J. Llopis, J.M. McCaffery, A. Miyawaki, M.G. Farquhar, R.Y. Tsien, Measurement of cytosolic, mitochondrial, and Golgi pH in single living cells with green fluorescent proteins. Proc. Natl. Acad. Sci. U. S. A. 95 (12) (1998) 6803-6808, https://doi.org/10.1073/pnas.95.12.6803.

[40] J.-T. Hou, K. Li, J. Yang, K.-K. Yu, Y.-X. Liao, Y.-Z. Ran, Y.-H. Liu, X.-D. Zhou, X.-Q. Yu, A ratiometric fluorescent probe for *in situ* quantification of basal mitochondrial hypochlorite in cancer cells. Chem. Commun. 51 (31) (2015) 6781-6784, https://doi.org/10.1039/C5CC01217A.

[41] C. Wang, S. Vegna, H. Jin, B. Benedict, C. Lieftink, C. Ramirez, R.L. Oliveira, B. Morris, J. Gadiot, W. Wang, A. Chatinier, L. Wang, D. Gao, B. Evers, G. Jin, Z. Xue, A. Schepers, F. Jochems, A.M. Sanchez, S. Mainardi, H. Riele, R.L. Beijersbergen, W. Qin, L. Akkari, R. Bernards, Inducing and exploiting vulnerabilities for the treatment of liver cancer, Nature 574 (2019) 268-272, https://doi.org/10.1038/s41586-019-1607-3.